PNAS Nexus, 2024, 3, pgae229
https://doi.org/10.1093/pnasnexus/pgae229
Advance access publication 12 June 2024
Research Report

Gradual ER calcium depletion induces a progressive and reversible UPR signaling

Ilaria Pontisso[a,1], Roberto Ornelas-Guevara[b,1], Eric Chevet[c,d], Laurent Combettes[a,*] and Geneviève Dupont[b,*]

[a]U1282 "Calcium Signaling and Microbial Infections", Institut de Biologie Intégrative de la Cellule (I2BC)—Université Paris-Saclay, Gif-Sur-Yvette 91190, France
[b]Unit of Theoretical Chronobiology, Université Libre de Bruxelles (ULB), 1050 Brussels, Belgium
[c]Inserm U1242 Université de Rennes, 35000 Rennes, France
[d]Centre de Lutte Contre le Cancer Eugène Marquis, 35042 Rennes, France
*To whom correspondence should be addressed: Email: laurent.combettes@universite-paris-saclay.fr; genevieve.dupont@ulb.be
[1]I.P. and R.O.-G. contributed equally to this work.
Edited By: JoAnn Trejo

Abstract

The unfolded protein response (UPR) is a widespread signal transduction pathway triggered by endoplasmic reticulum (ER) stress. Because calcium (Ca^{2+}) is a key factor in the maintenance of ER homeostasis, massive Ca^{2+} depletion of the ER is a potent inducer of ER stress. Although moderate changes in ER Ca^{2+} drive the ubiquitous Ca^{2+} signaling pathways, a possible incremental relationship between UPR activation and Ca^{2+} changes has yet to be described. Here, we determine the sensitivity and time-dependency of activation of the three ER stress sensors, inositol-requiring protein 1 alpha (IRE1α), protein kinase R-like ER kinase (PERK), and activating transcription factor 6 alpha (ATF6α) in response to controlled changes in the concentration of ER Ca^{2+} in human cultured cells. Combining Ca^{2+} imaging, fluorescence recovery after photobleaching experiments, biochemical analyses, and mathematical modeling, we uncover a nonlinear rate of activation of the IRE1α branch of UPR, as compared to the PERK and ATF6α branches that become activated gradually with time and are sensitive to more important ER Ca^{2+} depletions. However, the three arms are all activated within a 1 h timescale. The model predicted the deactivation of PERK and IRE1α upon refilling the ER with Ca^{2+}. Accordingly, we showed that ER Ca^{2+} replenishment leads to the complete reversion of IRE1α and PERK phosphorylation in less than 15 min, thus revealing the highly plastic character of the activation of the upstream UPR sensors. In conclusion, our results reveal a dynamic and dose-sensitive Ca^{2+}-dependent activation/deactivation cycle of UPR induction, which could tightly control cell fate upon acute and/or chronic stress.

Keywords: ER stress, calcium signaling, computational modeling, UPR reversion

Significance Statement

Partial endoplasmic reticulum (ER) calcium (Ca^{2+}) depletion and activation of unfolded protein response (UPR) are features observed in several human disease, but the relationship between these two phenomena and the sensitivity of UPR to Ca^{2+} decrease have not been extensively explored. In this work, we demonstrate how the UPR sensors show high plasticity in sensing physiological alterations by closely reporting the variations in ER Ca^{2+} levels. Using a mathematical model, we predicted the deactivation of protein kinase R-like ER kinase (PERK) and inositol-requiring protein 1 alpha (IRE1α) upon refilling the ER with Ca^{2+}. This prediction was confirmed experimentally revealing that ER Ca^{2+} replenishment led to the complete dephosphorylation of IRE1α and PERK in a few minutes. These results demonstrate how cell rapidly adapt to stress response signaling pathways to variations in ER homeostasis.

Introduction

Many physiological processes are modulated by the variation in intracellular concentration of calcium ions (Ca^{2+}) (1). Ca^{2+} is accumulated in the major intracellular store, the endoplasmic reticulum (ER) where it helps to maintain ER functions. Alteration of ER Ca^{2+} homeostasis leads to the accumulation of improperly folded proteins in the ER lumen, leading to a situation known as ER stress. To cope with this, cells have evolved an adaptive signaling pathway aiming at restoring ER homeostasis. This mechanism is collectively named the unfolded protein response (UPR) and is operated by the activation of three ER transmembrane proteins: the protein kinase R-like ER kinase (PERK), the inositol-requiring protein 1 alpha (IRE1α, referred to IRE1 hereafter), and the activating transcription factor 6 alpha (ATF6α, referred to ATF6 hereafter), which activate three parallel signal transduction pathways (2). In nonstressed conditions, sensors are maintained inactive through at least their binding to ER chaperone BiP. Upon accumulation of improperly folded proteins in the ER, BiP dissociates from

Competing Interest: E.C. is a founding member of Thabor Therapeutics.
Received: September 28, 2023. **Accepted:** May 29, 2024

the UPR sensors allowing for their activation and that of the downstream signaling pathways (3, 4). In addition, it has also been shown that the luminal domains of both IRE1 and PERK are able to bind to unfolded peptides, suggesting the existence of a direct sensing mechanism (5–7). To study UPR signaling, one of the most used ER stress inducers is linked to the depletion of luminal ER Ca^{2+}, generally obtained using inhibitors of the SERCA pumps (e.g. thapsigargin). Although these experiments have allowed significant advances in the understanding of the mechanisms underlying the activation of the UPR sensors and their downstream signals, they failed so far in exploring the tight relationships between ER Ca^{2+} concentrations and UPR activation especially when it comes to the sensitivity and early activation of the UPR by moderate and more physiological luminal Ca^{2+} stores modulation (8, 9). In this work, by combining experimental and mathematical modeling approaches, we have explored how UPR sensor activation closely reports the ER Ca^{2+} depletion in a gradual and reversible manner.

Results

Partial calcium depletion in the ER incrementally and reversibly activates the UPR sensors

To assess the impact of gradual ER Ca^{2+} store depletion on UPR activation, we used a reversible SERCA2B inhibitor at various concentrations. 2,5-di(*tert*-butyl)-1,4-benzohydroquinone (tBuBHQ) has a relatively low potency as compared to the more commonly used thapsigargin, with an IC_{50} in the range of 1 to 2 µM (10, 11). We monitored the kinetics of $[Ca^{2+}]_{ER}$ using GEM-CEPIA1er, the ratiometric version of CEPIA1er (12). This genetically encoded indicator has a K_D of 558 µM and a good dynamic range (R_{max}/R_{min} = 21.7). When expressed in HeLa cells, GEM-CEPIA1er correctly localized to the ER (Fig. 1a) and accurately reported changes in $[Ca^{2+}]_{ER}$ either upon treatment of the cells with histamine (Fig. 1b) or in response to SERCA2B pump inhibition by supramaximal dose of tBuBHQ (Fig. 1c). At lower concentrations, a dose-dependent plateau in $[Ca^{2+}]_{ER}$ was reached in less than 1 h. As compared to the $[Ca^{2+}]_{ER}$ decrease induced upon treatment with 30 µM tBuBHQ, $[Ca^{2+}]_{ER}$ was stabilized at 50, 60, and 85% of this value upon treatments with 3, 5, and 10 µM tBuBHQ, respectively. As shown in Fig. 2a and b, the evolution of $[Ca^{2+}]_{ER}$ upon treatment with tBuBHQ was consistent with kinetic simulations (see the Materials and methods section for a description of the model), taking into account the 2 µM IC50 of tBuBHQ binding to SERCA pumps (10, 11). As such, we next investigated if the graded decreases in $[Ca^{2+}]_{ER}$ impacted on different levels of ER stress.

High ER Ca^{2+} concentration plays a key role in the activity of many ER luminal chaperones and foldases (13), that, if not properly functioning, lead to ER protein homeostasis imbalance and UPR activation (14). BiP is one of the most abundant ER chaperones, which can bind a variety of substrates/clients. Given that measurement of global levels of misfolded proteins is technically very challenging, we followed BiP's mobility after treatment with tBuBHQ as a read-out of ER crowding. Fluorescence recovery after photobleaching (FRAP) experiments indeed revealed that ER stress induced by Tunicamycin or DTT treatment reduces BiP's mobility in FRAP, suggesting an increased ability of BiP to bind to larger proteins and aggregates (15). To evaluate the changes in BiP mobility that could result from the ER Ca^{2+} reduction induced upon treatment with tBuBHQ, we used HeLa cells

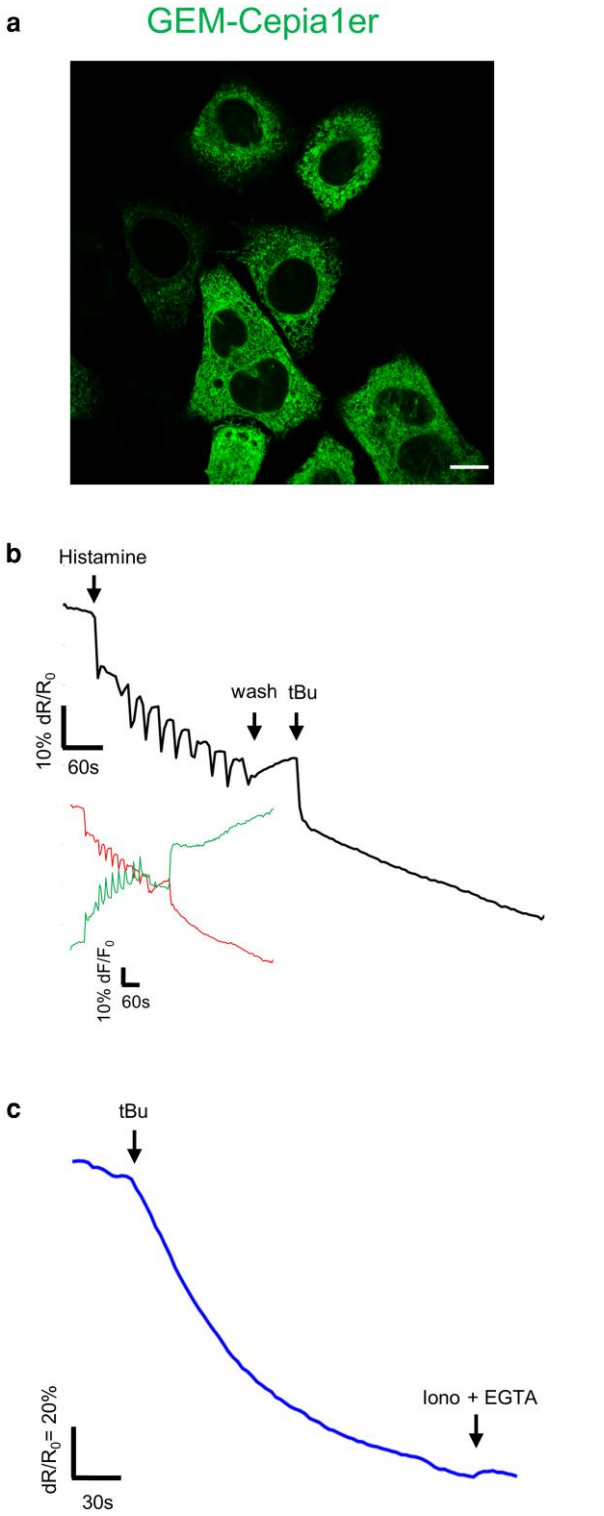

Fig. 1. tBuBHQ-mediated Calcium depletion in the ER. a) HeLa cells expressing GEM-CEPIA1er as analyzed using confocal microscopy. Scale bar = 10 µm. b) Representative Ca^{2+} traces obtained in HeLa cells expressing GEM-CEPIA1er Ca^{2+} indicator treated successively with histamine 50 µM and 30 µM tBuBHQ. Black trace reports ratio values between emission wavelengths F_{480}/F_{535}, red and green traces report fluorescence variation at 480 and 535 nm, respectively. c) Representative Ca^{2+} traces obtained in HeLa cells expressing GEM-CEPIA1er and treated with 30 µM tBuBHQ. After plateau was reached, cells were treated with Ionomycin (Iono) 2 µM and EGTA 20 mM as controls.

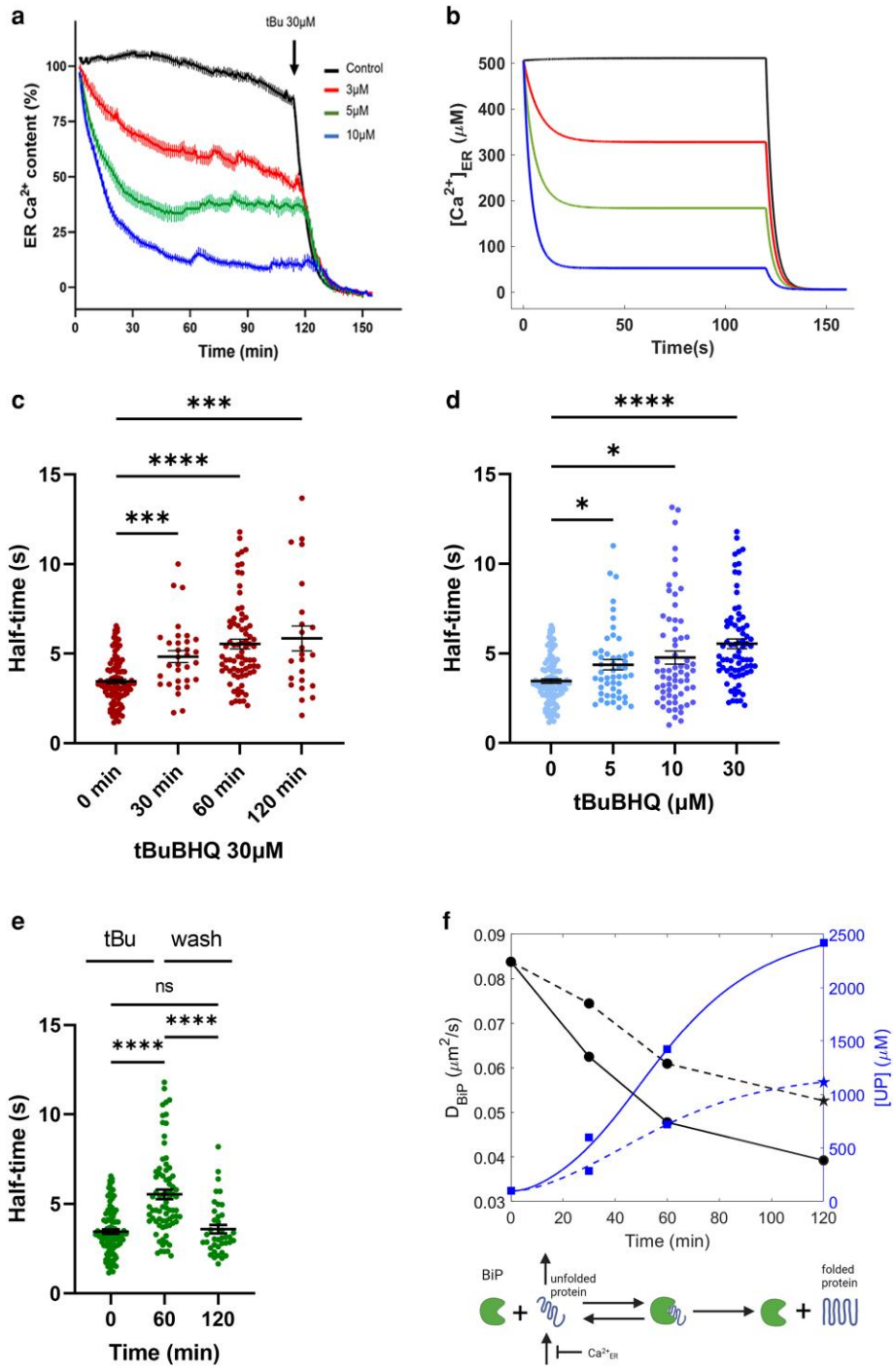

Fig. 2. ER calcium concentration-dependent BiP diffusion in the ER. a) HeLa cells expressing GEM-CEPIA1er were treated with indicated concentration of tBuBHQ (tBu). Percentage of ER Ca^{2+} was calculated from ratio of emission wavelengths values (F480/F535). Data display mean ± SEM of $n = 117$ (control), $n = 66$ (3 μM), $n = 32$ (5 μM), $n = 36$ (10 μM), ($N = 3$). b) Computational simulation of the time evolution of ER Ca^{2+} concentration after the addition of the tBu inhibitor for 2 h at different concentrations (3 μM, [red]; 5 μM, [green]; 10 μM, [blue]) as in (a). At 2 h, addition of 30 μM tBuBHQ is simulated for all conditions. c) Half-time values resulting from FRAP analyses performed in HeLa cells expressing BiP-mGFP and treated with 30 μM tBuBHQ for the indicated times. Data display mean ± SEM of $n = 102$ ($N = 5$), $n = 32$ ($N = 2$), $n = 76$ ($N = 5$), $n = 23$ ($N = 2$); $^{***}P \leq 0.001$; $^{****}P \leq 0.0001$; Kruskal–Wallis test with multiple comparisons post hoc test. d) Half-time values resulting from FRAP analyses performed in HeLa cells expressing BiP-mGFP and treated with the indicated doses of tBuBHQ for 1 h. Data display mean ± SEM of $n = 102$ ($N = 5$), $n = 50$ ($N = 2$), $n = 65$ ($N = 3$), $n = 76$ ($N = 5$); $^{*}P \leq 0.05$; $^{****}P \leq 0.0001$; Kruskal–Wallis test with multiple comparisons post hoc test. e) Half-time values resulting from FRAP analyses performed in HeLa cells expressing BiP-mGFP and treated with 30 μM tBuBHQ for 1 h. Cells were then washed twice with imaging medium and placed in complete medium for another hour before additional FRAP measurements. Data display mean ± SEM of $n = 102$ ($N = 5$), $n = 76$ ($N = 5$), $n = 39$ ($N = 2$); NS = $P > 0.05$; $^{****}P \leq 0.0001$; Kruskal–Wallis test with multiple comparisons post hoc test. f) Computational evaluation of BiP's effective diffusion coefficients (black lines) and of the corresponding concentrations of unfolded proteins (blue lines) in conditions of treatment with 30 μM (solid lines) and 10 μM (dashed lines) tBuBHQ, based on the half-times of recovery of fluorescence after photobleaching (c and d). The blue curves represent the simulated evolution of UP, using Eqs. (5)–(8) described in the Materials and methods section. Dots correspond to values of the diffusion coefficients evaluated from the half-times using Eq. (3), and squares to the concentrations of unfolded proteins based on Eq. (4). The stars indicate the model-predicted value of the diffusion coefficient and accumulated unfolded proteins after 2 h treatment with 10 μM tBuBHQ.

expressing BiP-mGFP (15) and evaluated the mobility of this protein using FRAP. We successively evaluated the time- and dose-dependencies of BiP mobility. Expression of BiP-mGFP per se did not induce ER stress nor UPR activation (Fig. S1). Under basal conditions, the half-time of BiP-mGFP recovery in the photobleached areas was of 3.45 ± 0.12 s (Fig. 2c). After treatment with 30 µM tBuBHQ, this value increased with time ($t_{1/2}$ = 4.83 ± 0.33 s after 30 min, $t_{1/2}$ = 5.54 ± 0.26 s after 1 h and $t_{1/2}$ = 5.85 ± 0.69 s after 2 h). The dose-dependency of BiP-mGFP mobility was assessed by treating cells with incremental doses of tBuBHQ for 1 h (Fig. 2d), revealing a decrease in BiP mobility with the concentration of the SERCA inhibitor ($t_{1/2}$ = 4.36 ± 0.28 s for 5 µM treatment, $t_{1/2}$ = 4.76 ± 0.36 s for 10 µM, and $t_{1/2}$ = 5.54 ± 0.26 s for 30 µM). The effects of tBuBHQ on BiP-mGFP mobility were also observed in Hela cells expressing BiP-mCherry, suggesting that the effect on the mobility of the protein of interest is not impacted by the fluorescent reporter used (Fig. S3). To test whether the observed decreases in BiP mobility could be due to changes in ER morphology, we stained HeLa cells for calnexin to visualize the ER structure. As shown in Fig. S2, these experiments did not reveal major structural ER changes after 2 h treatment with 30 µM tBuBHQ. Because higher doses and longer times after tBuBHQ treatment were associated with larger depletion of ER Ca^{2+} (Fig. 2a), we concluded that BiP mobility, and thus the accumulation of improperly folded proteins, are sensitive to $[Ca^{2+}]_{ER}$. In agreement with this, the half-time of BiP-mGFP recovery in the photobleached areas returned to values observed in nontreated cells in washout experiments on samples treated with maximal doses of SERCA inhibitor (Fig. 2e). Because the removal of tBuBHQ led to replenishment of the ER Ca^{2+} stores and restored basal ER homeostasis conditions, this observation confirms that BiP mobility dynamically adjusts to alterations of ER Ca^{2+} content.

To quantify the rate of accumulation of improperly folded proteins (UP), we generated a data-driven mathematical model of the $t_{1/2}$ of recovery after photobleaching. The diffusion coefficients were inferred from the half-times, either by explicit simulations of the FRAP experiments or by using an approximate equation that relates the two quantities. Assuming that BiP diffuses more slowly when bound to improperly folded proteins and that this association increases with the amount of misfolded proteins present in the ER lumen, this allowed us to determine a relative concentration of improperly folded proteins (Fig. 2f). These values were in agreement with the temporal evolution of [UP] predicted by a simple model assuming that ER Ca^{2+} is necessary for correct protein folding and taking into account the observed evolution of $[Ca^{2+}]_{ER}$ (Fig. 2f low panel and Eqs (5)–(8) in the Materials and methods section). The model also revealed the existence of a delay between the decrease in $[Ca^{2+}]_{ER}$ and UP accumulation. The correspondence between the model and the independent computational analysis of BiP diffusion $t_{1/2}$ pointed to an adequate quantification of the concentrations of UP or, at least, of their relative values. In conclusion, treatment of HeLa cells with appropriate concentrations of tBuBHQ allowed for a fine-tuned control of the rates and levels of depletion of ER Ca^{2+} depletion and subsequent accumulation of improperly folded proteins, thereby providing a modular system to explore ER Ca^{2+} impact on activation of the UPR.

Moderate ER Ca^{2+} depletion triggers activation of the three UPR pathways with different sensitivities and kinetics

Since we focus on the early activation of UPR, we monitored early markers of UPR induction that precede transcriptional and translational responses. Given that activation of both IRE1 and PERK depends on their autophosphorylation following oligomerization, we monitored their phosphorylation status using Phos-tag SDS PAGE and Western blot with anti-IRE1 and anti-PERK antibodies (16). Figure 3a shows that the phosphorylation patterns of IRE1 and PERK were distinct: IRE1 displayed a single slow migrating band upon induction while PERK activation resulted in several bands likely to reflect multiple phosphorylation. By quantifying the amount of phosphorylated sensor over total protein quantity, we determined the percentage of sensor activation after treatment with different concentrations of tBuBHQ. Under basal conditions, HeLa cells displayed a phosphorylation status of about 15% for both IRE1 and PERK (Fig. 3b). For these two sensors, tBuBHQ induced an increase in phosphorylation in a dose dependent manner suggesting that the pattern of sensor activation correlates with the extent of ER Ca^{2+} depletion. Notably, IRE1 phosphorylation reached its maximal level at 1 h post treatment for all doses tested and then plateaued at a level proportional to the extent of ER depletion (Fig. 2b). In comparison, PERK phosphorylation was slower and kept increasing gradually over the duration of the experiment (2 h). Moreover, the extent of phosphorylation after 2 h was significantly higher for 30 µM tBuBHQ than for lower doses. PERK activation thus appeared to be slower and less sensitive to Ca^{2+} depletion than IRE1 in our experimental setup.

To monitor ATF6 activation, HeLa cells expressing pEGFP-ATF6 were live-imaged upon ER stress induction with tBuBHQ. Immunofluorescence experiments for colocalization with giantin (Golgi complex marker) revealed an increased fluorescence in the Golgi complex upon ER stress (Fig. 3c). Quantification of Golgi/ER intensity ratios revealed a dose-dependent ATF6 activation, as for the other sensors (Fig. 3d). Kinetics was similar to those obtained for PERK, while dose sensitivity appeared bimodal with similar patterns for the two lowest and the two highest tBuBHQ concentrations. Moreover, treatment with maximal dose of tBuBHQ for 2 h induces cleavage of ATF6 (Fig. S5), suggesting that Golgi accumulation is quickly followed by ATF6 cleavage in the time frame considered. These results reveal that ER luminal Ca^{2+} concentration decrease is detected by the three UPR sensors thus impacting on the three branches of the UPR in an hour time. Moreover, IRE1, PERK, and ATF6 are activated at different rates and sensitivities, suggesting different characteristics of activation by the increase in [UP] triggered by the decrease in $[Ca^{2+}]_{ER}$, a mechanism that might be cell-type specific.

IRE1 and PERK activation is reversible upon repletion of ER Ca^{2+}

To gain insight into the possible mechanisms controlling the initial activation kinetics and sensitivities of the three branches of the UPR, we developed minimal computational models describing IRE1, PERK, and ATF6 activation. These models, schematized in Fig. 4a and b, assume the existence of preformed oligomers of IRE1 and PERK and describe activation of the sensors upon dissociation of BiP. Bip-free IRE1 and PERK can autophosphorylate. For ATF6, the free sensor can translocate to the Golgi apparatus. For each branch, the evolution of BiP concentration is imposed by the changes in ER Ca^{2+} concentration shown in Fig. 2b. In the absence of available information about the kinetic constants, we used the genetic algorithm for optimization of the parameters provided in the COPASI software (17) (Fig. 4c). It predicts that IRE1 has a lower affinity for BiP and autophosphorylates in larger oligomers than PERK. Because the molecular steps involved in the

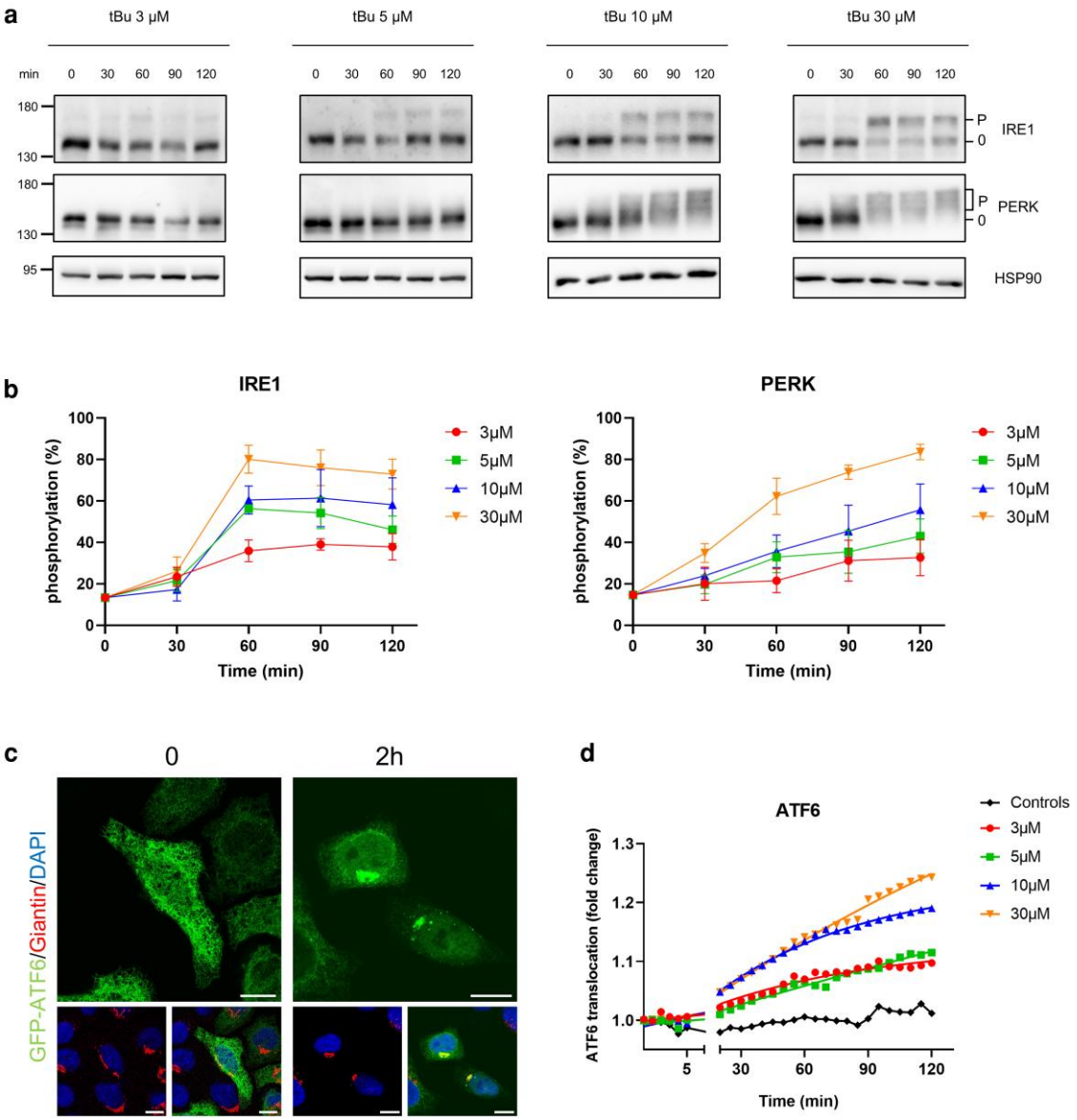

Fig. 3. Incremental activation of the UPR sensors upon calcium depletion in the ER. a) HeLa cells were treated with the indicated concentrations of tBu. PERK and IRE1 phosphorylation status was monitored using Phos-tag SDS-PAGE and Western blot. b) Quantification of results presented in (a) reported in percentage of phosphorylated protein over the total PERK/IRE1 protein quantity (mean ± SEM of $N = 3$). c) ATF6 subcellular colocalization with Giantin (Golgi) and DAPI (nucleus) following treatment with 30 µM tBuBHQ for the indicated time. Scale bar = 10 µm. d) Quantification of ATF6 translocation to the Golgi following treatment with the indicated doses of tBuBHQ. Values of Golgi/reticular intensity ratio were normalized to basal values observed before the addition of tBuBHQ. Mean of $n = 45$ (control), $n = 43$ (3 µM), $n = 39$ (5 µM), $n = 22$ (10 µM), $n = 51$ (30 µM) ($N = 3$). SEM was omitted for the sake of clarity (data are provided in Fig. S4).

model for IRE1 and PERK are all reversible, it is implicitly considered in the models that the inductions of the branches should be reversible if $[Ca^{2+}]_{ER}$ is brought back to its initial value. To assess the validity of this assumption, we used the model to predict the evolution of the levels of phosphorylated sensors upon washing of the reversible SERCA inhibitor tBuBHQ. As shown in Fig. 4d, in the presence of external Ca^{2+}, $[Ca^{2+}]_{ER}$ is predicted to increase rather rapidly, reaching about 80% of its full content in ~30 min, with a slower rate of replenishment afterwards. Concomitantly, the levels of phosphorylation of both IRE1 and PERK both decrease and tend to recover their basal levels (Fig. 4e).

To validate this prediction, we imaged $[Ca^{2+}]_{ER}$ changes as described above in response to a 90 min treatment with 30 µM tBuBHQ, followed by washout. The steep decrease in $[Ca^{2+}]_{ER}$ was followed by store replenishment displaying biphasic kinetics (Fig. 5a). In another set of experiments, we monitored IRE1 and PERK phosphorylation status in cells subjected to the tBuBHQ treatments (Fig. 5b). As predicted by the model, drug washout resulted in a decrease in the amount of the phosphorylated sensors, which both reach their basal level in about 1 h, thus mirroring the evolution of $[Ca^{2+}]_{ER}$ recovery (Fig. 5b and c). However, deactivation of IRE1 and PERK was surprisingly faster in the experiments than in the model, with half-times of restoration equal to 15.4 and 14 min for IRE1 and PERK, respectively, instead of 74 and 20 min in the simulations. Moreover, the return to pretreatment activation/phosphorylation levels was faster for IRE1 than for PERK, in contrast to the model's predictions. In the model, the faster return of PERK was likely due to its larger affinity for BiP, which is in agreement with the observed faster activation of the IRE1 branch.

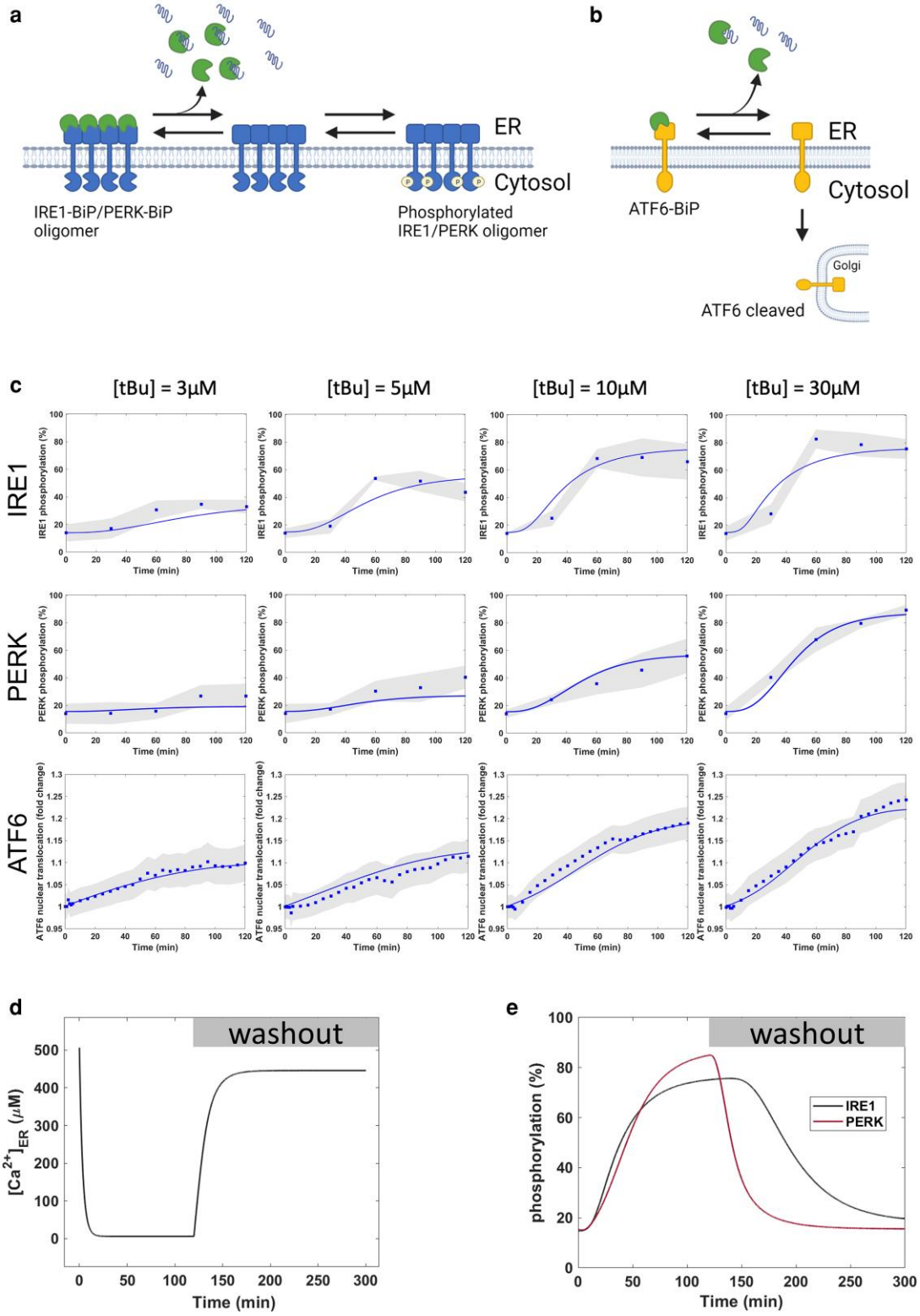

Fig. 4. Data-driven computational simulation of IRE1, PERK, and ATF6 activation. a) Schematic representation of the model of activation of IRE1 and PERK based on the dissociation of BiP from the sensors upon accumulation of UP. The modes of activation are assumed to be similar for IRE1and PERK, although the two differ by the values of the kinetic constants. The model assumes the existence of preformed oligomers of IRE1 and PERK. Equations of the model are given in the Materials and methods section. b) Schematic representation of the model of activation of ATF6 based on the dissociation of BiP upon accumulation of UP. When freed from BiP, ATF6 translocates to the Golgi complex where it is cleaved by S1P and S2P. Equations of the model are given in the Materials and methods section. c) Computational simulations of the activation of the 3 branches of the UPR after treatment with different concentrations of tBu. Blue lines correspond to the results of the simulations of the models schematized in a and b, with the Eqs. (1), (2), (5)–(15) and the parameter values listed in Table S1. Blue squares represent experimental data and the grey shaded region, the curve interpolated between those data ± SEM. d) Model prediction of the evolution of ER Ca^{2+} concentration after washout of tBu 30 μM. In the model Eqs. (1) and (2), tBu concentration is multiplied by 0.05 at time 120 min. e) Model prediction of the reversion of IRE1 and PERK activation after washout of tBu 30 μM, corresponding to the evolution of $[Ca^{2+}]_{ER}$ shown in (d). Results were obtained by integration of Eqs. (1), (2), (5)–(12).

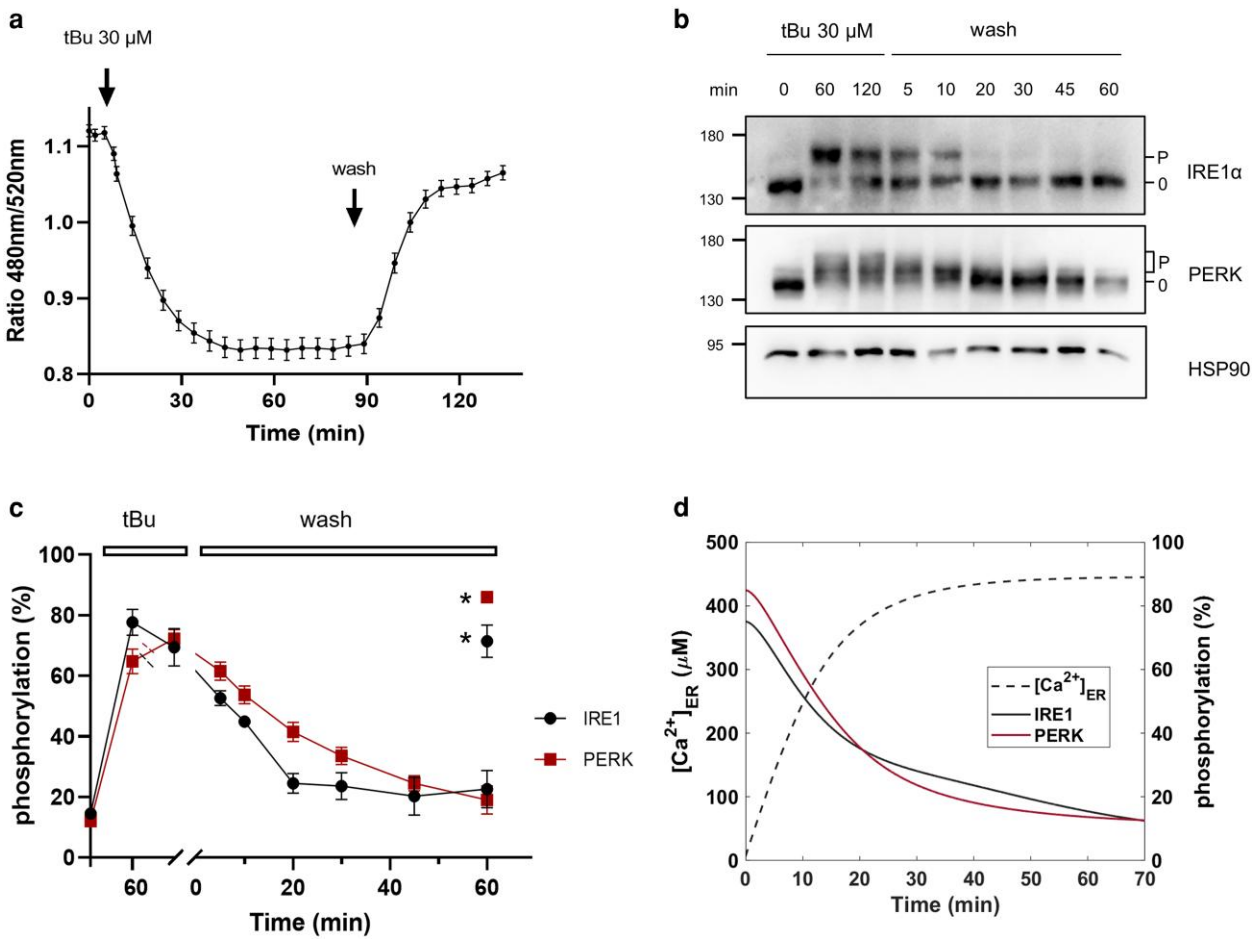

Fig. 5. Reversible activation of the UPR sensors upon ER calcium restoration. a) HeLa cells expressing GEM-Cepia1er Ca^{2+} were treated with 30 µM tBu for 90 min then washed twice to remove all traces of SERCA inhibitor. The graph shows ratio values between emission wavelengths F480/F535 (mean ± SEM of $n = 46$). b) HeLa cells were treated with 30 µM tBu for 2 h and washed twice before being incubated in normal culture medium. PERK and IRE1 phosphorylation status was monitored using Phos-tag SDS-PAGE/Western blot. c) Quantification of results presented in (b) as percentage of phosphorylated protein over the total PERK/IRE1 protein quantity (mean ± SEM of $N = 4$). Asterisks (*) at 60 min indicate IRE1 and PERK values when tBu treatment was maintained for the entire duration of the experiment and no washing was performed. d) Model simulation of the faster reversion of IRE1 and PERK activation after washout of tBu 30 µM when taking into account a possible Ca^{2+} activation of the IRE1 and PERK phosphatases. Results have been obtained with Eqs (1), (2), (5)–(11), (16) with the evolution of $[Ca^{2+}]_{ER}$ shown in Fig. 4d.

Such discrepancies in the recovery times cannot be alleviated by changing the ratios between the values of the rate constants of phosphorylation and dephosphorylation but point to the existence of an additional mechanism that regulates IRE1 and PERK recovery. Accordingly, when considering the activation of a phosphatase activity by Ca^{2+}, simulations are able to account for the observed fast recovery (Fig. 5d).

In summary, experimental observations and modeling indicate that the three branches of UPR are initiated with different kinetics that can be ascribed to differences in the early steps following BiP unbinding. Hence, the activation status of the IRE1 and PERK UPR sensors rapidly mirrors the variations in $[Ca^{2+}]_{ER}$ upon both depletion or restoration.

Discussion

In this work, we show that gradual ER luminal Ca^{2+} depletion results in increased production and accumulation of improperly folded proteins and that UPR induction is triggered even in conditions in which the ER Ca^{2+} content is only partially reduced. This approach differs from the classical studies on UPR activation in which massive depletion of Ca^{2+} is maintained over a long period using the irreversible SERCA inhibitor thapsigargin. Previous studies explored the relationship between moderate depletion of ER Ca^{2+} and induction of the UPR (8, 9). In contrast with our work, these studies did neither specifically focus on the immediate activation of the sensors nor on the mechanism that allows the UPR transducers to sense luminal Ca^{2+} alteration. Moreover, our experimental investigation was accompanied by mathematical modeling. Similar approaches already allowed characterizing the kinetics and cross-regulations between the three UPR branches (18), but until now no model has focused on the first steps of UPR induction in response to moderate changes in Ca^{2+} concentration.

Herein, the application of different doses of tBuBHQ led to intermediate ER Ca^{2+} steady states that more closely recapitulate possible Ca^{2+} alterations likely relevant to both physiological and pathological contexts. UPR sensors readily respond to Ca^{2+} variations with different kinetics and sensitivities. The model considers BiP titration-dependent sensors' activation and predicts a lower affinity of IRE1 for BiP compared to PERK. This could explain the faster activation kinetics of IRE1 in response to Ca^{2+} depletion compared to PERK and suggests that IRE1 more rapidly responds to BiP dissociation than PERK. Indeed, reduction in ER Ca^{2+} concentration negatively influences BiP's ability to bind to client proteins and

therefore also to sensors (19, 20). The model also suggests the existence of larger oligomers of IRE1 than PERK, which relates to a more progressive activation of the latter sensor. Previous studies have shown that ER stress sensors could exist in preformed complexes at the ER membrane and upon ER stress would form even larger structures (21, 22). Our model suggests that dimerization/oligomerization step does not play a key part in the activation of IRE1 and PERK sensor when it comes to a BiP titration-dependent activation. Decreases in BiP mobility were considered as a proxy for the accumulation of improperly folded proteins in the ER. While this is in line with previous studies (15), it has also been demonstrated that BiP forms oligomers which can participate to the regulation of BiP active monomers. Ca^{2+} depletion favors oligomer formation and detachment from substrates (20) thereby allowing the cell to respond more readily to Ca^{2+} fluctuations by regulating BiP accessibility. It is therefore possible that the Ca^{2+} dependent reduction in BiP mobility that we observed in our FRAP experiments is partially due to formation of BiP oligomers. However, BiP binding to unfolded proteins and BiP oligomerization both lead to a decrease in the amount of available BiP monomers, which is the only quantity that is assumed to regulate UPR activation in our model. Thus, regardless of the relative contribution of unfolded proteins binding or oligomer formation, our data document relative values for the accumulation of misfolded proteins with ER Ca^{2+} depletion. Interplay between BiP luminal diffusion and control of ER Ca^{2+} concentration could also be considered in a more detailed modeling approach. Indeed, diffusion of luminal Ca^{2+}-binding proteins, particularly those with low affinity Ca^{2+}-binding sites such as BiP, favors localized release of ER Ca^{2+} (23), and simulations suggest that immobilized Ca^{2+} buffers decrease the speed of Ca^{2+} ions release (23).

To our knowledge, this work is the first to closely explore the reversion of UPR sensor activation in conditions of ER Ca^{2+} replenishment. Ca^{2+} dependent induction of ER stress is generally obtained by treatment with thapsigargin, which inhibits SERCA pumps in an irreversible manner and therefore is not suited to explore reversion phenotypes. Previous studies have shown that washout of cyclopiazonic acid, another reversible SERCA2B inhibitor, results in ER stress resolution, and restoration of PERK sensor activation but without having a close look at the kinetics (24–26). In the present study, we found that SERCA2B inhibitor washout reversed IRE1 and PERK phosphorylation in less than 1 h, mirroring very closely the kinetics of Ca^{2+} store replenishment and suggesting that these proteins sense luminal Ca^{2+} levels very well. Such a rapid reversion indicated that there could be an induction of a Ca^{2+} sensitive phosphatase involved in the dephosphorylation of the sensors. A well-documented Ca^{2+} sensitive cytoplasmic phosphatase is calcineurin. It has been shown that calcineurin can associate with active PERK in the presence of high Ca^{2+}, so presumably soon after ER stress induction by SERCA pump inhibition. This interaction increases PERK phosphorylation and plays a role in PERK downstream signaling (27). At this stage, it is difficult to rule out that another phosphatase could be responsible for the deactivation of the sensors. Of note, our knowledge regarding phosphatases that counteract the activation of UPR sensors IRE1 and PERK is very limited, although some phosphatases have been shown to dephosphorylate IRE1 in yeast and mammals (28–31). In addition, a ER localized tyrosine phosphatase, PTP-1B, has been shown to regulate IRE1 signaling and *Xbp1* mRNA splicing via dephosphorylation of RtcB ligase (32, 33) as well as the PERK pathway (34, 35). Importantly, it has been shown that PTP-1B is negatively regulated by Ca^{2+} influx through TRPV1 and via store-operated Ca^{2+} entry (SOCE) mechanisms (36, 37).

Inactivation of the UPR sensors still remains largely unexplored and current research mainly focuses on the most conserved sensor IRE1. Indeed, IRE1 is negatively regulated by a complex formation with antiapoptotic protein BAX inhibitor-1 (38) and by direct binding with PDIA6 which acts on possible disulfide formation to stabilize oligomers, a mechanism also found for PERK (39). In addition, some other studies have suggested that reversion of sensors' activation could be finely tuned by modulation of their oligomeric status and its association with BiP via Sec61 and the Sec63 translocon proteins (40, 41). It might be possible that restoration of ER luminal Ca^{2+} impacts and accelerates these processes. Along this line, we showed here that the observed fast reversion of IRE1 and PERK activation is best described by the model when taking into account an activation of the phosphatase activity by Ca^{2+}. This activation would take place at the phosphorylation sites of the sensor located on the cytoplasmic side of the ER membrane, where significant fluxes are supposed to occur upon store replenishment. The high SOCE activity is indeed at the origin of microdomains in which Ca^{2+} concentrations can become larger than in the rest of the cytoplasm (42). Our work did not explore reversion of activation occurring at the level of ATF6 sensor. Our experiment monitors translocation of ATF6 to the Golgi complex while the models assume that the pool of translocated sensor is immediately cleaved by Golgi proteases to reach the nucleus, as also suggested by the results presented in Fig. S5. However, we cannot exclude that restoration of ER Ca^{2+} levels could impact on the downregulation of ATF6 signaling via modulation of retrograde transport, the inhibitory binding to BiP or redox dependent ATF6 dimerization (43) or through the fact that that ATF6 is a natively unstable protein in the ER (44, 45).

In conclusion, our work documents the tight relationships existing between ER Ca^{2+} concentrations and the activation of the three UPR transducers. The combined use of experimental approaches and mathematical modeling has allowed us to describe for the first time a rapid mechanism of IRE1 and PERK deactivation upon Ca^{2+} replenishment in the ER lumen which could explain the very high plasticity of the UPR upon physiological management of ER stress.

Materials and methods

Cell culture and treatments

Hela cells were cultured in RPMI medium (Gibco-Thermo Fischer Scientific) supplemented with 10% FBS (Gibco 10270 -Thermo Fischer Scientific) at 37°C in a 5% CO_2 incubator. tBuBHQ was purchased from Sigma Aldrich (112976) and dissolved in DMSO. Cells were treated with the corresponding concentrations of tBuBHQ for the indicated times.

Transfection and plasmids

Plasmid transfections were carried out 24 h after cell plating (except when otherwise indicated) using FuGENE HD Transfection Reagent (Promega), following manufacturer's instructions. After 6 h, cells were washed with phosphate-buffered saline (PBS) for two times and fresh culture medium was added. pCIS GEM-CEPIA1er (#58217), peGFP-ATF6 (#32955), BiP-mGFP (#62231), and BiP-mCherry (#62233) were purchased from Addgene.

Live imaging for calcium measurements and ATF6 translocation

HeLa cells seeded on 25 mm coverslips and transfected with pCIS GEM-CEPIA1er or peGFP-ATF6 24 and 48 h after plating,

respectively. Cells were placed in an observation chamber in imaging medium containing 115 mM NaCl, 5.6 mM KCl, 1.8 mM $CaCl_2$, 1.2 mM $MgCl_2$, 1 mM $NaHPO_4$, 10 mM $NaHCO_3$, 20 mM HEPES (pH = 7.4), and 1 mg/mL glucose. Samples were analyzed at room temperature on an inverted Nikon eclipse TE200 fluorescence microscope, using a 60× objective. Illuminating sources used were ex. 380 nm; em. 480 nm/535 nm for GEM-CEPIA1er and ex. 485 nm; em. 535 nm for GFP-ATF6 driven by Simple 32 Software from Compix Incorporated. Images were captured using a CMOS camera (Hamamatsu). Images were analyzed with Simple 32 software. Changes in the ratio of GEM-CEPIA1er were transformed into ER Ca^{2+} percentage by taking the mean intensity value at resting conditions as 100% and lower value as 0%. Fold change of GFP-ATF6 translocation was calculated by dividing Golgi intensity values by ER intensity values for each time point.

Cell manipulations and Western blot analyses

To obtain total cell extracts cells were lysed in sample buffer 1× (62.5 mM Tris pH = 8, 2% SDS, 10% glycerol, 0.05% bromophenol blue, 5% β-mercaptoethanol), sonicated and boiled at 95°C for 5 min. Proteins from total lysates were separated by SDS PAGE or Phos-tag SDS PAGE as reported in Ref. (16) and transferred to nitrocellulose membrane (0.45 µM Amersham Protran). Western blot analyses were performed according to standard procedure using the following primary antibodies: PERK (Cell Signaling Technologies C33E10), IRE1α (Cell Signaling Technologies 14C10), HSP90 (Santa Cruz Biotechnologies sc-13119), and GFP (Roche 11814460001). HRPO conjugated anti-mouse (Cytiva) and anti-rabbit (Sigma) were used as secondary antibodies.

Immunofluorescence analyses

After fixation with paraformaldehyde (PFA), cells were permeabilized with 0.01% Triton X-100 for 5 min. Samples were washed three times with PBS and blocked with PBS containing 3% FBS for 30 min. Cells were incubated for 2 h with primary mouse antibody against giantin (1:200) (Abcam 37266) or primary rabbit antibody against calnexin (1:200) (Sigma C4731). Cells were incubated with the corresponding secondary IgG antibodies for 1 h. Samples were mounted in Dako mounting medium (DAKO) and analyzed using a Nikon Ti2 confocal microscope with a 60× objective, controlled by Nikon software.

FRAP experiments

Cells were cultured on 25-mm-diameter coverslips and transfected with BiP-mGFP or BiP-mCherry 24 h before performing the experiment. Cells were mounted in an observation chamber in imaging medium (see above). Experiments were performed using an inverted spinning disk confocal microscopy (Gataca system) and analyzed with a 100× objective, using an sCMOS camera (Photometrics) equipped with a FRAP module and driven by the Metamorph software (Roper Scientific Instruments), allowing to the acquisition of images during the bleaching phase. Samples were treated with different doses of tBuBHQ for the indicated times or left untreated. For each sample, bleaching and image acquisition were performed using identical conditions. Bleaching was performed for 50 ms using 50% of maximal laser power. Twenty and 300 acquisitions were taken every 50 ms pre- and post-bleaching, respectively. Fluorescence curves were corrected for background levels and for fluorescence bleaching. Normalized recovery curves were fitted using easyFRAP for MATLAB (46).

Statistical analyses

Data are expressed as mean ± SEM of three independent experiments unless differently indicated. Differences were statistically analyzed using Prism 7 (GraphPad). *P*-values <0.05 were considered significant.

Model description

Calcium dynamics

Ca^{2+} is pumped from the cytosol into the ER through the SERCA pump. The latter is inhibited by tBuBHQ (tBu), with a K_D value equal to 2 µM (10). In the opposite way, Ca^{2+} leaks from the ER into the cytosol. Ca^{2+} exchanges between the cytoplasm and the extracellular medium are mediated by the plasma membrane Ca^{2+} ATPase (PMCA) that extrudes Ca^{2+} out of the cell and by SOCE, a STIM/ORAI-mediated mechanism that is sensitive to the Ca^{2+} concentration inside the ER. The resulting changes in ER (C_{ER}) and cytosolic (C_c) Ca^{2+} concentrations are given by the following equations (47):

$$\frac{dC_{ER}}{dt} = \alpha\left(V_e \frac{C_c^2}{C_c^2 + K_e^2} \cdot \frac{K_I^n}{tBu^n + K_I^n} - k_{out}[C_{ER} - C_c]\right) \quad (1)$$

$$\frac{dC_c}{dt} = k_{out}[C_{ER} - C_c] - V_e \frac{C_c^2}{C_c^2 + K_e^2} \cdot \frac{K_I^n}{tBu^n + K_I^n} - V_p \frac{C_c^2}{C_c^2 + K_p^2} + V_S \frac{K_S^4}{C_{ER}^4 + K_S^4}. \quad (2)$$

Definitions and default values of the parameters are listed in Table S1.

Estimation of the effective diffusion coefficients of BiP and of the related concentrations of unfolded proteins

FRAP experiments were performed after different times of treatment of HeLa cells with tBu 30 µM and revealed distinctive half-times of recovery of BiP-associated fluorescence (Fig. 2c). The observed step-up in the half-times reflects the increasing binding of unfolded proteins to BiP. To infer the value of the diffusion coefficient of BiP—representing a weighted average of free and UP-bound forms—from the measured values of half-times, we performed 3D simulations of diffusion of BiP molecules at a concentration of 100 µM (48), surrounding an empty hole with the same radius as the photobleached region. We looked for the values of D_{BIP} allowing to obtain half-times of recovery corresponding to observations. For each experimental point (corresponding to a given time after tBu treatment, see Fig. 2c), best agreement was always close to the expected value with the measured half-times, i.e. with

$$D_{BIP} = 0.224 \cdot \frac{r_n^2}{t_{1/2}}, \quad (3)$$

where r_n is the radius of the uniform bleach laser and $t_{1/2}$ the measured half-time (49).

From these effective diffusion coefficients, the corresponding concentrations of UP can be evaluated by

$$[UP] = \frac{D_{BIP}^0 - D_{BIP}}{D_{BIP} - D_{UP}}\left(\frac{(K + [BiP])^2}{K}\right). \quad (4)$$

This equation is analogous to that used to quantify the decrease in the effective diffusion coefficient of Ca^{2+} (the "equivalent" of BiP) in the presence of Ca^{2+} buffers (the "equivalent" of UP). In Eq. (4), D_{BIP}^0 stands for the diffusion coefficient of free BiP, D_{UP} for the diffusion coefficient of an average UP in the ER and *K*, for the

dissociation constant of UP from BiP. The value of D^0_{BIP} was estimated from half-time at time 0 (Fig. 2c) and D_{UP} was calculated using the Einstein–Stokes relation and was found to be equal to 0.009086727 $\mu m^2\ s^{-1}$, considering a hydrodynamic radius equal to 0.035 μm (50). [BiP] was taken equal to 100 μM (48) and K, to 8.7 μM (51).

Activation of the UPR sensors

Activation of the three branches of the UPR is triggered independently by BiP unbinding from the corresponding sensors. In conditions of a full ER and in the absence of stress inducer corresponding to a low concentration of unfolded proteins (UP) in the ER, IRE1, PERK, and ATF6 sensors are bound to BiP. The relation between ER Ca^{2+} changes and BiP dynamics is schematized in Fig. 1D. It is assumed that unfolded protein (UP) production in the ER is inhibited by ER Ca^{2+}, as a simplified way of representing the Ca^{2+} dependence of protein chaperons and foldases. UP bind to BiP with high affinity. This initiates the folding process, after which free BiP is recovered. The model also allows for the possibility of incomplete protein folding, in which case BiP is freed together with the modified UP. Corresponding evolution equations are:

$$\frac{d\mathrm{UP}}{dt} = \upsilon_{\mathrm{prod}} \cdot P_{\mathrm{UP}} - k_{\mathrm{BU}} \cdot \mathrm{BiP} \cdot \mathrm{UP} + k_2 \cdot \mathrm{BiP\text{–}UP} - k_d \cdot \mathrm{UP} \tag{5}$$

$$\frac{d\mathrm{BiP}}{dt} = (k_1 + k_2) \cdot \mathrm{BiP\text{–}UP} - k_{\mathrm{BU}} \cdot \mathrm{BiP} \cdot \mathrm{UP} \tag{6}$$

$$\frac{d\mathrm{BiP\text{–}UP}}{dt} = k_{\mathrm{BU}} \cdot \mathrm{BiP} \cdot \mathrm{UP} - (k_1 + k_2) \cdot \mathrm{BiP\text{–}UP} \tag{7}$$

$$\frac{dP_{\mathrm{UP}}}{dt} = \frac{1}{\tau_{\mathrm{UP}}}\left(\frac{K_{\mathrm{ER}}}{C_{\mathrm{ER}} + K_{\mathrm{ER}}} - P_{\mathrm{UP}}\right) \tag{8}$$

where UP, BiP, and BiP-UP stand for the concentrations of unfolded proteins, free BiP and UP-bound BiP, respectively. P_{UP} is a function that modulates the production of UP, depending on the concentration of ER Ca^{2+}. Parameter τ_{UP} accounts for a possible delay between ER Ca^{2+} decrease and accumulation of UP. Equations (5)–(7) correspond to the mass action law description of the mechanism schematized in Fig. 2d. Definitions and default values of the parameters are listed in Table S1.

We assume that the activation of the IRE1 and PERK sensors obey the same mechanisms (Fig. 4a) but differ in their kinetics, i.e. involve different rate constants. Thus, in the following description, the term "sensor" stands for IRE1 or for PERK. Preformed oligomers of the sensor are supposed to be present in the ER membrane (21, 22). S represents the concentration of BiP-unbound, unphosphorylated oligomers. These oligomers can bind BiP, with a stoichiometry that corresponds to the size of the oligomer. As the sensor can be free (S), bound to BiP (BiP-S) or phosphorylated (S_p), the conservation relation for the sensor reads:

$$S_{\mathrm{tot}} = S + \mathrm{BiP\text{–}S} + S_p. \tag{9}$$

We assume rapid equilibrium on the reactions of BiP binding and unbinding to and from the sensors, i.e.

$$n_{\mathrm{SB}} \cdot k^+_{\mathrm{SB}} \cdot (S_{\mathrm{tot}} - S_P - \mathrm{BiP\text{–}S}) \cdot \mathrm{BiP}^n = n_{\mathrm{SB}} \cdot k^-_{\mathrm{SB}} \cdot \mathrm{BiP\text{–}S}. \tag{10}$$

The rate of change of the concentration of sensor oligomers due to phosphorylation and dephosphorylation is given by:

$$\frac{dS_P}{dt} = k_{\mathrm{sk}} S - k_{\mathrm{sp}} S_p, \tag{11}$$

where k_{Sk} and k_{Sp} stand for the rate constants of the kinase and the phosphatase, respectively.

Changes in the concentration of phosphorylated sensor can be described by a single differential equation:

$$\frac{dS_P}{dt} = \frac{1}{\tau_{\mathrm{SP}}}\left(S_{\mathrm{tot}} \cdot K_{\mathrm{sp}} \cdot \frac{K^{\mathrm{ns}}_{\mathrm{SB}}}{\mathrm{BiP}^{\mathrm{ns}} + K^{\mathrm{ns}}_{\mathrm{SB}}} - S_P\right). \tag{12}$$

In Eq. (12), τ_{SP} is the inverse of the rate constant of dephosphorylation, i.e. $1/k_{sp}$. S_{tot} stands for the total concentration of oligomers of the sensor, K_{Sp} for the ratio between the first order kinetic constants of phosphorylation (k_{Sk}) and dephosphorylation (k_{sp}), and K_{SB} for the ratio between the unbinding (k^-_{SB}) and binding (k^+_{SB}) rate constants of BiP from and to the sensor. The Hill-type factor follows the assumption of rapid equilibrium for BiP binding and unbinding to and from the sensor, with ns being the number of monomers that form an oligomer. It is also assumed that the concentration of phosphorylated sensor is much smaller than the total concentration of sensor ($S_P << S_{tot}$) given that we model early and moderate activation of UPR. Table S1 lists the values of the parameters, with the "S" being replaced by "I" and "P" for the IRE1 and PERK pathways, respectively.

Similarly, activation of the ATF6 branch of UPR follows the unbinding of BiP from this sensor. This triggers the cleavage of ATF6 and its translocation to the Golgi, as schematized in Fig. 4b. Thus, the evolutions of BiP-bound, free and translocated ATF6 are given by the following equations:

$$\frac{d\mathrm{A\text{–}BiP}}{dt} = k^+_{\mathrm{AB}} \cdot \mathrm{A} \cdot \mathrm{BiP} - k^-_{\mathrm{AB}} \cdot \mathrm{A\text{–}BiP} \tag{13}$$

$$\frac{d\mathrm{A}}{dt} = k^-_{\mathrm{AB}} \cdot \mathrm{A\text{–}BiP} - k^+_{\mathrm{AB}} \cdot \mathrm{A} \cdot \mathrm{BiP} - k_{\mathrm{AC}} \cdot \mathrm{A} \tag{14}$$

$$\frac{dA_c}{dt} = k_{\mathrm{AC}} \cdot \mathrm{A} - k_{\mathrm{dAC}} \cdot A_c. \tag{15}$$

Definitions and values of the parameters are listed in Table S1.

Model extension to account for the observed fast kinetics of reversion

Although the model qualitatively predicted reversion of IRE1 and PERK activation, the simulated dephosphorylation of the two sensors was slower than in the experiments (compare Figs. 4e and 5c). We therefore extended the model to take into account the possibility that a Ca^{2+} sensitive phosphatase participates in the inactivation of the sensors. Such phosphatase activity has progressively accumulated near the sensors during their activation. The rate constant of the phosphatase k_{sp} (Eq. 9) now reads:

$$k_{\mathrm{sp}} = \overline{k_{\mathrm{sp}}}\left(1 + \alpha_{\mathrm{sr}} \frac{C_{\mathrm{ER}}}{K_{\mathrm{sr}} + C_{\mathrm{ER}}}\right). \tag{16}$$

The Ca^{2+} concentration in the ER is taken as a proxy for the Ca^{2+} concentration on the cytoplasmic side of the ER membrane where the phosphorylation sites of the sensors are located. Definitions and default values of the parameters are listed in Table S1.

Acknowledgments

The authors acknowledge the contribution of Simon Le Goupil for his help in the analysis of ATF6 cleavage.

Supplementary Material

Supplementary material is available at *PNAS Nexus* online.

Funding

This work was supported by the Fonds de la Recherche Scientifique - FNRS (PDR T.0073.21 F) to G.D., ANR-20-CE15-0001-0001 CALPLYCX to L.C., Institut National du Cancer (PLBIO2019, PLBIO2020, PLBIO2022), and Fondation pour la Recherche Médicale (DEQ20180339169, EQU202403018041) to E.C. G.D. is Research Director at the Belgian "Fonds National pour la Recherche Scientifique" (FRS-FNRS). I.P. was funded by a PhD scholarship from the French ministry of research. The present work has benefited from Imagerie-Gif core facility supported by ANR-11-EQPX-00297Morphoscope, ANR-10-INBS-04/FranceBioImaging, ANR-11-IDEX.0003-02/Saclay Plant Sciences.

Author Contributions

L.C. and G.D. initiated the project. I.P. and L.C. performed all in vivo experiments and data analysis. R.O.-G. and G.D. established and performed the modeling experiments. E.C. contributed to the experimental design, data analysis, and manuscript writing. I.P. and G.D. wrote the article with input from all authors.

Data Availability

All data are included in the manuscript and/or supporting information. Western blot raw data are stored at Figshare: DOI 10.6084/m9.figshare.25977151. The code used in this manuscript is stored in GitHub: https://github.com/RobertoOrnelasGuevara/UPR_calcium.

References

1 Bootman MD, Bultynck G. 2020. Fundamentals of cellular calcium signaling: a primer. *Cold Spring Harb Perspect Biol*. 12: a038802.
2 Almanza A, *et al*. 2019. Endoplasmic reticulum stress signalling—from basic mechanisms to clinical applications. *FEBS J*. 286: 241–278.
3 Bertolotti A, Zhang Y, Hendershot LM, Harding HP, Ron D. 2000. Dynamic interaction of BiP and ER stress transducers in the unfolded-protein response. *Nat Cell Biol*. 2:326–332.
4 Shen J, Chen X, Hendershot L, Prywes R. 2002. ER stress regulation of ATF6 localization by dissociation of BiP/GRP78 binding and unmasking of Golgi localization signals. *Dev Cell*. 3:99–111.
5 Credle JJ, Finer-Moore JS, Papa FR, Stroud RM, Walter P. 2005. On the mechanism of sensing unfolded protein in the endoplasmic reticulum. *Proc Natl Acad Sci USA*. 102:18773–18784.
6 Karagöz GE, *et al*. 2017. An unfolded protein-induced conformational switch activates mammalian IRE1. *Elife*. 6:e30700.
7 Wang P, Li J, Tao J, Sha B. 2018. The luminal domain of the ER stress sensor protein PERK binds misfolded proteins and thereby triggers PERK oligomerization. *J Biol Chem*. 293:4110–4121.
8 Szalai P, *et al*. 2018. Nonlinear relationship between ER $Ca^{(2+)}$ depletion versus induction of the unfolded protein response, autophagy inhibition, and cell death. *Cell Calcium*. 76:48–61.
9 Paredes RM, Bollo M, Holstein D, Lechleiter JD. 2013. Luminal Ca^{2+} depletion during the unfolded protein response in Xenopus oocytes: cause and consequence. *Cell Calcium*. 53:286–296.
10 Kass GE, Duddy SK, Moore GA, Orrenius S. 1989. 2,5-Di-(tert-butyl)-1,4-benzohydroquinone rapidly elevates cytosolic Ca2+ concentration by mobilizing the inositol 1,4,5-trisphosphate-sensitive Ca^{2+} pool. *J Biol Chem*. 264:15192–15198.
11 Moore GA, McConkey DJ, Kass GE, O'Brien PJ, Orrenius S. 1987. 2,5-Di(tert-butyl)-1,4-benzohydroquinone–a novel inhibitor of liver microsomal Ca^{2+} sequestration. *FEBS Lett*. 224:331–336.
12 Suzuki J, *et al*. 2014. Imaging intraorganellar Ca^{2+} at subcellular resolution using CEPIA. *Nat Commun*. 5:4153.
13 Krebs J, Agellon LB, Michalak M. 2015. $Ca^{(2+)}$ homeostasis and endoplasmic reticulum (ER) stress: an integrated view of calcium signaling. *Biochem Biophys Res Commun*. 460:114–121.
14 Carreras-Sureda A, Pihan P, Hetz C. 2018. Calcium signaling at the endoplasmic reticulum: fine-tuning stress responses. *Cell Calcium*. 70:24–31.
15 Lai CW, Aronson DE, Snapp EL. 2010. Bip availability distinguishes states of homeostasis and stress in the endoplasmic reticulum of living cells. *Mol Biol Cell*. 21:1909–1921.
16 Yang L, *et al*. 2010. A phos-tag-based approach reveals the extent of physiological endoplasmic reticulum stress. *PLoS One*. 5:e11621.
17 Hoops S, *et al*. 2006. COPASI—a COmplex PAthway SImulator. *Bioinformatics*. 22:3067–3074.
18 Pontisso I, Ornelas-Guevara R, Combettes L, Dupont G. 2023. A journey in UPR modelling. *Biol Cell*. 115:2200111.
19 Preissler S, *et al*. 2015. Physiological modulation of BiP activity by trans-protomer engagement of the interdomain linker. *Elife*. 4: e08961.
20 Preissler S, *et al*. 2020. Calcium depletion challenges endoplasmic reticulum proteostasis by destabilising BiP-substrate complexes. *Elife*. 9:e62601.
21 Sundaram A, Appathurai S, Plumb R, Mariappan M. 2018. Dynamic changes in complexes of IRE1α, PERK, and ATF6α during endoplasmic reticulum stress. *Mol Biol Cell*. 29:1376–1388.
22 Belyy V, Zuazo-Gaztelu I, Alamban A, Ashkenazi A, Walter P. 2022. Endoplasmic reticulum stress activates human IRE1α through reversible assembly of inactive dimers into small oligomers. *Elife*. 11:e74342.
23 Crapart CC, *et al*. 2024. Luminal transport through intact endoplasmic reticulum limits the magnitude of localized $Ca^{(2+)}$ signals. *Proc Natl Acad Sci USA*. 121:e2312172121.
24 Fumagalli F, *et al*. 2016. Translocon component Sec62 acts in endoplasmic reticulum turnover during stress recovery. *Nat Cell Biol*. 18:1173–1184.
25 Guan B-J, *et al*. 2017. A unique ISR program determines cellular responses to chronic stress. *Mol Cell*. 68:885–900.e6.
26 Chen C-W, *et al*. 2022. Adaptation to chronic ER stress enforces pancreatic β-cell plasticity. *Nat Commun*. 13:4621.
27 Bollo M, *et al*. 2010. Calcineurin interacts with PERK and dephosphorylates calnexin to relieve ER stress in mammals and frogs. *PLoS One*. 5:e11925.
28 Chang T-K, *et al*. 2018. Coordination between two branches of the unfolded protein response determines apoptotic cell fate. *Mol Cell*. 71:629–636.e5.
29 Qiu Y, *et al*. 2010. A crucial role for RACK1 in the regulation of glucose-stimulated IRE1alpha activation in pancreatic beta cells. *Sci Signal*. 3:ra7.
30 Welihinda AA, Tirasophon W, Green SR, Kaufman RJ. 1998. Protein serine/threonine phosphatase Ptc2p negatively regulates the unfolded-protein response by dephosphorylating Ire1p kinase. *Mol Cell Biol*. 18:1967–1977.
31 Guo J, Polymenis M. 2006. Dcr2 targets Ire1 and downregulates the unfolded protein response in *Saccharomyces cerevisiae*. *EMBO Rep*. 7:1124–1127.
32 Gu F, *et al*. 2004. Protein-tyrosine phosphatase 1B potentiates IRE1 signaling during endoplasmic reticulum stress. *J Biol Chem*. 279:49689–49693.

33 Papaioannou A, *et al.* 2022. Stress-induced tyrosine phosphorylation of RtcB modulates IRE1 activity and signaling outputs. *Life Sci Alliance*. 5:e202201379.

34 Bettaieb A, *et al.* 2012. Protein tyrosine phosphatase 1B deficiency potentiates PERK/eIF2α signaling in brown adipocytes. *PLoS One*. 7:e34412.

35 Bakke J, Haj FG. 2015. Protein-tyrosine phosphatase 1B substrates and metabolic regulation. *Semin Cell Dev Biol*. 37: 58–65.

36 Bogeski I, Bozem M, Sternfeld L, Hofer HW, Schulz I. 2006. Inhibition of protein tyrosine phosphatase 1B by reactive oxygen species leads to maintenance of Ca^{2+} influx following store depletion in HEK 293 cells. *Cell Calcium*. 40:1–10.

37 de Jong PR, *et al.* 2014. Ion channel TRPV1-dependent activation of PTP1B suppresses EGFR-associated intestinal tumorigenesis. *J Clin Invest*. 124:3793–3806.

38 Lisbona F, *et al.* 2009. BAX inhibitor-1 is a negative regulator of the ER stress sensor IRE1alpha. *Mol Cell*. 33:679–691.

39 Eletto D, Eletto D, Dersh D, Gidalevitz T, Argon Y. 2014. Protein disulfide isomerase A6 controls the decay of IRE1α signaling via disulfide-dependent association. *Mol Cell*. 53:562–576.

40 Sundaram A, Plumb R, Appathurai S, Mariappan M. 2017. The Sec61 translocon limits IRE1α signaling during the unfolded protein response. *Elife*. 6:e27187.

41 Li X, *et al.* 2020. A molecular mechanism for turning Off IRE1α signaling during endoplasmic reticulum stress. *Cell Rep*. 33:108563.

42 Guse AH, Gil Montoya DC, Diercks B-P. 2021. Mechanisms and functions of calcium microdomains produced by ORAI channels, d-myo-inositol 1,4,5-trisphosphate receptors, or ryanodine receptors. *Pharmacol Ther*. 223:107804.

43 Oka OBV, *et al.* 2022. Activation of the UPR sensor ATF6α is regulated by its redox-dependent dimerization and ER retention by ERp18. *Proc Natl Acad Sci USA*. 119:e2122657119.

44 Papaioannou A, *et al.* 2018. Alterations of EDEM1 functions enhance ATF6 pro-survival signaling. *FEBS J*. 285:4146–4164.

45 Ninagawa S, *et al.* 2015. Forcible destruction of severely misfolded mammalian glycoproteins by the non-glycoprotein ERAD pathway. *J Cell Biol*. 211:775–784.

46 Rapsomaniki MA, *et al.* 2012. easyFRAP: an interactive, easy-to-use tool for qualitative and quantitative analysis of FRAP data. *Bioinformatics*. 28:1800–1801.

47 Dupont G, Falcke M, Kirk V, Sneyd J. 2016. Models of calcium signalling. In: Dupont G, Falcke M, Kirk V, Sneyd J, editors. *Interdisciplinary applied mathematics*. Switzerland: Springer International Publishing. p. 295–336.

48 Roth RA, Koshland ME. 1981. Role of disulfide interchange enzyme in immunoglobulin synthesis. *Biochemistry*. 20:6594–6599.

49 Axelrod D, Koppel DE, Schlessinger J, Elson E, Webb WW. 1976. Mobility measurement by analysis of fluorescence photobleaching recovery kinetics. *Biophys J*. 16:1055–1069.

50 Nicoud L, Lattuada M, Yates A, Morbidelli M. 2015. Impact of aggregate formation on the viscosity of protein solutions. *Soft Matter*. 11:5513–5522.

51 Carrara M, Prischi F, Nowak PR, Kopp MC, Ali MM. 2015. Noncanonical binding of BiP ATPase domain to Ire1 and Perk is dissociated by unfolded protein CH1 to initiate ER stress signaling. *Elife*. 4:e03522.